Solid State Sciences 80 (2018) 72–80

Contents lists available at ScienceDirect

Solid State Sciences

journal homepage: www.elsevier.com/locate/ssscie

On the novel double perovskites $A_2Fe(Mn_{0.5}W_{0.5})O_6$ (A= Ca, Sr, Ba). Structural evolution and magnetism from neutron diffraction data

Crisanto A. García-Ramos [a, b], Sebastián Larrégola [c], María Retuerto [d], María Teresa Fernández-Díaz [e], Kiril Krezhov [b], José Antonio Alonso [a, *]

[a] Instituto de Ciencia de Materiales de Madrid, Consejo Superior de Investigaciones Científicas (C.S.I.C.), Cantoblanco, E-28049 Madrid, Spain
[b] Institute for Nuclear Research and Nuclear Energy (I.N.R.N.E.), Tsarigradsko Chaussee 72, BG-1784 Sofia, Bulgaria
[c] INTEQUI, CONICET, 5700 San Luis, Argentina
[d] Instituto de Catálisis y Petroleoquímica, Consejo Superior de Investigaciones Científicas (C.S.I.C.), Cantoblanco, E-28049 Madrid, Spain
[e] Institut Laue Langevin, BP 156X, Grenoble, F-38042, France

ARTICLE INFO

Article history:
Received 23 March 2018
Accepted 28 March 2018
Available online 29 March 2018

Keywords:
Double perovskite
Tolerance factor
Anti-site disordering
Neutron diffraction
Sr_2FeMoO_6

ABSTRACT

New $A_2Fe(Mn_{0.5}W_{0.5})O_6$ (A = Ca, Sr, Ba) double perovskite oxides have been prepared by ceramic techniques. X-ray diffraction (XRD) complemented with neutron powder diffraction (NPD) indicate a structural evolution from monoclinic (space group $P2_1/n$) for A = Ca to cubic ($Fm\text{-}3m$) for A = Sr and finally to hexagonal ($P6_3/mmc$) for A = Ba as the perovskite tolerance factor increases with the A^{2+} ionic size. The three oxides present different tilting schemes of the FeO_6 and $(Mn,W)O_6$ octahedra. NPD data also show evidence in all cases of a considerable anti-site disordering, involving the partial occupancy of Fe positions by Mn atoms, and vice-versa. Magnetic susceptibility data show magnetic transitions below 50 K characterized by a strong irreversibility between ZFC and FC susceptibility curves. The A = Ca perovskite shows a G-type magnetic structure, with weak ordered magnetic moments due to the mentioned antisite disordering. Interesting magnetostrictive effects are observed for the Sr perovskite below 10 K.

1. Introduction

Iron oxides with double perovskite structure have attracted a lot of attention since 1998, when Kobayashi et al. [1] published that the Sr_2FeMoO_6 oxide was a ferromagnetic half-metal with Curie temperature (T_C) ~ 400 K, a saturation magnetization (M_S) = 3.1 μ_B at low temperature and presented magnetoresistance at room temperature (MR = 42% at 4.2 K and MR = 10% at 300 K both at 7 T fields). This paradigmatic compound has been synthesized and studied on numerous occasions, with the aim to optimize its properties and make it useful for possible applications. In 1999 Kim et al. [2] also observed intergranular magnetoresistance at room temperature; finding values of MR = 6% with an applied field of 1.5 T and M_S = 1.3 μ_B, although these authors did not study the cationic disorder. García-Landa et al. [3] synthesized the material by solid state reaction, treating the starting oxides at high temperatures in reducing flows, and obtained M_S = 2.2 μ_B and MR = 3.9% (applied field of 2 T and room temperature). Later on, a Monte Carlo simulation study [4] showed the influence of the disorder between Fe and Mo on the properties of the oxide; since then numerous articles have been published where the cationic disorder is related to the properties of the material. Niebieskikwiat et al. [5] obtained M_S = 2.7 μ_B and T_C ~ 405 K. Other studies illustrated the importance of the reduction step at high temperature in current of 1% H_2/Ar and obtained a compound with 4% of Fe atoms in Mo positions and M_S = 3.6 μ_B [6]. Further improvements [7,8] yielded Sr_2FeMoO_6 with 2% of disorder, M_S = 3.75 μ_B and T_C ~ 420 K. In a previous work we achieved an almost complete ordered Sr_2FeMoO_6 with M_S = 3.97 μ_B, MR = 45% at 5 K for H = 9 T and low-field MR = 6.5% at room temperature for H = 0.3 T [9].

Beyond Sr_2FeMoO_6, other $A_2FeB'O_6$ double perovskites (A = alkali-earth ions; B' = second or third-row transition metal) and derivatives were described [10–12]. Following this investigation, we were attracted by the study of novel oxides of stoichiometry $A_2Fe(Mn_{0.5}B''_{0.5})O_6$ where A = Ca, Sr, Ba; B" = W, Mo, Te and Re. In this series of compounds we are replacing half of the B′ atoms by Mn^{4+}, in a trial to enhance the magnetic interactions with the Fe sublattice. In the present work we address the

* Corresponding author.
E-mail address: ja.alonso@icmm.csic.es (J.A. Alonso).

https://doi.org/10.1016/j.solidstatesciences.2018.03.022
1293-2558/

preparation, structural and magnetic characterization of the $A_2Fe(Mn_{0.5}W_{0.5})O_6$ series. We have successfully prepared these new phases by ceramic procedures; a preliminary XRD study suggests that the A = Sr material is cubic (S.G. *Fm-3m*) whereas the Ca-containing sample is monoclinic (S.G. $P2_1/n$) and the Ba-containing oxide is hexagonal (S.G. $P6_3/mmc$). This is in agreement with the evolution of the tolerance factor when the A ion radius varies from Ca to Ba.

Due to the similarity between the X-ray scattering factors of Fe and Mn it is not possible to obtain information on the distribution of both cations between the two B-sublattices; the knowledge of the possible anti-site effect (Fe at Mn positions or viceversa) is of paramount importance for the interpretation of the magnetic properties. This is particularly feasible from NPD data, given the contrasting scattering lengths of Fe and Mn, of opposite sign. Therefore, we have performed a careful structural study of the three members of this family $A_2Fe(Mn_{0.5}W_{0.5})O_6$ with A = Ca, Sr and Ba (CFMW, SFMW and BFMW hereafter) from NPD data in order to confirm and refine the crystal structures at RT and low temperature and to study the eventual magnetic structures at low temperature, in complement with magnetization measurements.

2. Experimental section

$A_2Fe(Mn_{0.5}W_{0.5})O_6$ (A = Ca, Sr, Ba) perovskites were synthesized by solid state reaction between A $(NO_3)_2$ (A = Ca, Sr, Ba), Fe_2O_3, MnO_2 and WO_3 in the stoichiometric proportions. The mixtures were ground and calcined at 1000 °C for 24 h. Subsequently, the products were treated at 1200 °C for 6 h × 4 times with several interval regrindings. Finally the samples were calcined at 1300 °C for 12 h until single $A_2Fe(Mn_{0.5}W_{0.5})O_6$ phases were obtained. All the calcination steps were carried out in alumina crucibles and in air atmosphere.

The final materials were characterized by XRD for phase identification and for assessment of the phase purity using a Brucker D8 diffractometer (40 kV, 30 mA), controlled by a DIFFRACTPLUS software, in Bragg-Brentano reflection geometry with CuKα radiation (λ = 1.5418 Å), between 10 and 64 2θ degrees. NPD was also essential to characterize the subtle structural features concerning oxygen positions, octahedral tilting and Fe/Mn antisite disordering. For A = Sr, high-resolution patterns were collected in the 3T2 diffractometer at the LLB Institut, in Saclay (France), with λ = 1.2254 Å, and low-temperature data at G4.1 instrument (λ = 2.4226 Å) of the same Institut. The RT patterns for A = Ca, Ba were collected at the D1A diffractometer of the Institut Laue-Langevin, Grenoble, in the high-resolution configuration with a neutron wavelength λ = 1.91 Å. The low-temperature measurements were performed at D1B diffractometer with λ = 2.42 Å. In all cases, about 2 g of the samples were contained in vanadium cylinders. The NPD data were analyzed by the Rietveld method [13] with the FULLPROF program [14]. A pseudo-Voigt function was chosen to generate the line shape of the diffraction peaks. In the final run, the following parameters were refined: scale factor, background points, zero shift, half-width, pseudo-Voigt corrected for asymmetry parameters, unit-cell parameters, positional coordinates and isotropic displacement factors for all the atoms. The coherent scattering lengths of Ca, Sr, Ba, Fe, Mn, W and O were 4.70, 7.02, 5.07, 9.45, −3.73, 4.86, and 5.803 fm, respectively.

dc magnetic susceptibility measurements were carried out using a commercial (Quantum Design) SQUID magnetometer in the temperature range from 2 K to 400 K under a 0.1 T external magnetic field. The isothermal magnetization curves were obtained for magnetic fields going from −5 T to 5 T.

3. Results and discussion

3.1. Structural characterization at room temperature

The materials of the $A_2Fe(Mn_{0.5}W_{0.5})O_6$ (A = Ca, Sr, Ba) series were obtained as well-crystallized polycrystalline samples of dark-brown color. The XRD diagrams are characteristic of perovskite-type structure (Fig. 1), showing different types of superstructures and symmetries. No impurity phases were detected in the x-ray diagrams. Fig. 1 shows the Rietveld fits of XRD data considering the models derived from NPD data described below.

3.1.1. $Ca_2Fe(Mn_{0.5}W_{0.5})O_6$

The fine details of the crystal structure of $Ca_2Fe(Mn_{0.5}W_{0.5})O_6$ were refined from the high resolution NPD data collected at 295 K. It was refined using the monoclinic space group $P2_1/n$ (#14). This symmetry has been typically observed in most of the double perovskites containing Ca at the A-sublattice [15–17]. The unit-cell parameters are related to a_0 (ideal cubic perovskite, $a_0 \approx 3.8$ Å) as $a \approx \sqrt{2}a_0$, $b \approx \sqrt{2}a_0$, $c \approx 2a_0$, $\beta \approx 90°$. This space group considers two different crystallographic positions for the B and B′ octahedral cations in $A_2BB'O_6$, as well as 3 kinds of non-equivalent oxygen atoms (O1, O2 and O3), all in general positions. BO_6 and $B'O_6$ octahedra alternate along the three directions of the structure, in such a way that each BO_6 octahedron is linked to 6 $B'O_6$ octahedra, and vice-versa. The main component of the distortion from the ideal cubic perovskite structure corresponds to the tilt of the BO_6 octahedra, of the type $a^-a^-c^+$ in the Glazer's nomenclature, in the $P2_1/n$ space group. Table 1 contains the unit-cell parameters, atomic positions, isotropic displacement factors, occupancy and reliability factors of the refinement at 295 K. Table 2 lists the interatomic distances and some selected bond angles. An important anti-site effect was refined between the Fe at 2*a* sites and the Mn at 2b positions, considering that W was fully located at 2b sites, since a clear superstructure peak was observed at the XRD pattern at $2\theta = 19°$.

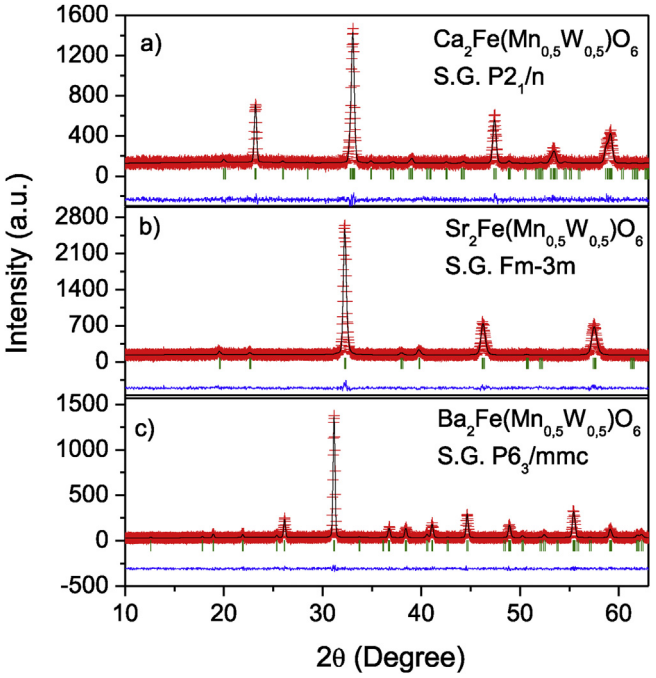

Fig. 1. Rietveld plots of a) $Ca_2Fe(Mn_{0.5}W_{0.5})O_6$; b) $Sr_2Fe(Mn_{0.5}W_{0.5})O_6$; c) $Ba_2Fe(Mn_{0.5}W_{0.5})O_6$ from laboratory x-ray data with CuK_α radiation.

Table 1
Unit cell, positional and displacement parameters for the compounds under study in the monoclinic $P2_1/n$ space group for CFMW, *Fm-3m* S.G. for SFMW and $P6_3/mmc$ for BFMW from NPD at 295 K.

S.G.		CFMW	SFMW	BFMW
		$P2_1/n$	*Fm-3m*	$P6_3/mmc$
a(Å)		5.40873 (16)	7.8434 (3)	5.74084 (9)
b(Å)		5.47457 (17)	= a	= a
c(Å)		7.68234 (25)	= a	14.05383 (3)
β(°)		90.03 (1)	90	γ = 120
Vol(Å^3)		227.477 (12)	482.522 (4)	401.120 (13)
R_p(%)		9.28	10.7	11.5
R_{wp}(%)		9.06	9.23	10.5
R_{exp}(%)		6.15	4.18	6.33
R_{BRAGG}(%)		3.59	1.99	4.66
χ^2		2.17	4.88	2.74
A	**x**	0.0079 (5)	¼	0
	y	0.0384 (3)	¼	0
	z	0.249 (3)	¼	¼
	B_{iso}(Å^2)	1.65 (6)	1.10 (2)	0.44 (9)
A2	**x**	–	–	1/3
	y	–	–	2/3
	z	–	–	0.5934 (2)
	B_{iso}(Å^2)	–	–	0.85 (9)
B1	**x**	½	0	0
	y	0	0	0
	z	0	0	0
	B_{iso}(Å^2)	0.5 (3)	0.29 (7)	0.81 (9)
B2	**x**	0	0	1/3
	y	½	0	2/3
	z	0	½	0.1487 (2)
	B_{iso}(Å^2)	0.8 (3)	0.57 (8)	0.4 (1)
O1	**x**	0.291 (1)	0.2506 (4)	0.4831 (1)
	y	0.291 (2)	0	0.9661 (2)
	z	0.035 (1)	0	¼
	B_{iso}(Å^2)	1.9 (1)	β_{11} = 75 (1) x 10^{-4} β_{22} = 75 (1) x10^{-4} β_{33} = 36 (2) x10^{-4} B_{eq} = 1.518	1.31 (5)
O2	**x**	0.296 (1)	–	0.1653 (1)
	y	0.292 (2)	–	0.3306 (1)
	z	0.457 (1)	–	0.4172 (1)
	B_{iso}(Å^2)	1.1 (1)	1.53 (1)	0.98 (4)
O3	**x**	0.9253 (3)	–	–
	y	0.4817 (3)	–	–
	z	0.249 (2)	–	–
	B_{iso}(Å^2)	1.47 (6)	–	–

The final crystallographic formula after the refinement was $Ca_2(Fe_{0.70(1)}Mn_{0.30(1)})_{2a}(Fe_{0.30(1)}Mn_{0.20(1)}W_{0.5})_{2b}O_6$. However, there is some extent of long range ordering between Fe and Mn, since Fe atoms are preferentially located at 2*a* octahedra, what allows us to consider it as a double perovskite structure. A total disordering would have required a refinement in the *Pbnm* space group where there would be a single octahedral B site containing the three different metal atoms distributed at random.

Fig. 2a displays the Rietveld plot illustrating the goodness of the fit between observed and calculated NPD data at RT. In the right panel a view of the crystal structure is shown, enhancing the rotation of the octahedra $(Fe,Mn)O_6$ and $(Fe,Mn,W)O_6$ in phase along the direction (001) of the pseudocubic cell and in antiphase along the directions (100) and (010). As it is expected, there are three types of Ψ (B-O-B′) bond angles. The average tilting angle can be estimated by θ = (180- Ψ)/2, in each crystal direction taking the values of $\theta_A = 12.20°$, $\theta_B = 13.75°$ and $\theta_C = 12.24°$. The monoclinic angle is very close to 90°, which indicates that the cell has a strong pseudo-orthorhombic character.

3.1.2. $Sr_2Fe(Mn_{0.5}W_{0.5})O_6$

Fig. 2b shows the results of the refinements from neutron diffraction data for the A = Sr sample. The XRD and NPD profiles shows a number of weak odd-odd-odd or F-type reflections such as 511 and 531, indicative of ordering of the Fe/Mn (NPD) and W (XRD) cations, which double the unit-cell size. The absence of any appreciable splitting of the Bragg reflections in the XRD and NPD profiles strongly suggests that this material is indeed cubic. The crystal structure was refined in the space group Fm-3m with a = 7.8433 (4) Å, twice the unit-cell parameter of the cubic perovskite aristotype.

Despite the experimental evidence of the absence of structural distortion from the cubic symmetry, the chance of a tetragonal distortion was considered, and some trial refinements in the *I*4/*m* space group were carried out. These attempts to fit the data to this model were unsatisfactory, since the tetragonality index (c/a) was always almost 1 (a = b = c) with the refinement invariably suggesting an unrealistic distortion of the BO_6 octahedra. The above-mentioned peculiarities plus the presence of an almost null tilting angle along the c direction (S.G. *I*4/*m* in perovskites is characterized by $a^0a^0b^-$ tilting system in the Glazer's notation) confirms the absence of tetragonal distortion and the cubic nature of the crystal structure. Fig. 2b shows the goodness of the Rietveld fit for the A = Sr sample refined in the cubic model. The right panel of Fig. 2b shows a view of the cubic superstructure. Table 1 lists the main atomic parameters after the refinement at RT, and Table 2 the main interatomic distances and angles.

There is only one variable structural parameter in the cubic structure, concerning the oxygen at 24*e* (x, 0, 0) sites, with x very close to ¼, related to the non-equivalent octahedral sizes. In the

Table 2
Main interatomic distances (Å) and angles (°) obtained for the P_α polymorphs at 295 K.

	CFMW	SFMW	BFMW
A-O Polyhedron			
A-O1	2.39 (3)	12 × 2.7730 (1)	6 × 2.8756 (7)
	2.64 (3)		
	2.65 (3)		
A-O2	2.34 (3)	–	6 × 2.8677 (3)
	2.63 (3)		
	2.69 (3)		
A-O3	2.468 (3)	–	–
	2.363 (4)		
<A-O>			2.8716
A-O Polyhedron			
A-O1	–	–	3 × 2.859 (2)
A-O2	–	–	3 × 2.987 (2)
			3 × 2.874 (1)
<A-O>	–	–	2.8988 (5)
B-O Polyhedron			
B-O1	2 × 1.979 (11)	6 × 1.966 (4)	6 × 2.0140 (4)
B-O2	2 × 1.991 (10)	–	–
B-O3	2 × 1.973 (16)	–	–
<B-O>	1.9801	1.966	2.0140
O1-B1-O1	180	180	–
O2-B1-O2	180	90	89.04 (4)
O1-B1-O2	91.2 (4)	90	–
O2-B1-O3	88.6 (2)	–	–
B′-O Polyhedron			
B2-O1 (x2)	2 × 1.958 (10)	6 × 1.956 (4)	3 × 2.059 (2)
B2-O2 (x2)	2 × 1.970 (10)	–	3 × 1.910 (1)
B2-O3 (x2)	2 × 1.958 (16)	–	–
<B2-O>	1.9619	1.956	1.9851 (7)
O1-B2-O1	180	180	77.50 (8)
O2-B2-O2	180	90	98.47 (7)
O1-B2-O2	90.0 (5)	90	91.09 (4)
O2-B2-O3	89.75 (19)	–	–
B1-O1-B2	155.6 (5)	180	–
B2-O1-B2	–	–	87.44 (17)
B1-O2-B2	152.5 (5)	180	173.71 (10)
B1-O3-B2	155.51 (10)	–	–
θ_A	12.20	–	
θ_B	13.75	–	
θ_C	12.24	–	

final refinement cycles, anisotropic displacement parameters were refined for the oxygen atoms, leading to a small increase in the quality of the fit with R_p decreasing from 11.2% to 10.7%, χ^2 from 5.36 to 4.88 and R_B from 2.31% to 1.99%. The displacement parameters for this atom appear to be flattened along the B-O-B bond direction, as it is expected, with equivalent isotropic displacement parameters of 1.52 $Å^2$.

For the refinement of the anti-site disorder, the W atoms were kept at the 4b sites (derived from the XRD analysis) and the mixed occupancy of Fe and Mn between 4*a* and 4b sites was refined from NPD data. An important value of anti-site disorder was found, implying that a considerable number of Fe atoms are at Mn nominal positions and vice-versa. The final refined stoichiometry can be re-written as $Sr2(Fe_{0.76(1)}Mn_{0.24(1)})_{4a}$ $(Fe_{0.24(1)}Mn_{0.26(1)}W_{0.5})_{4b}O_6$. In fact, if we analyze the stoichiometry and the disorder, it seems that the sample is acquiring the highest disorder value admitted between Mn and Fe, since the 4b site shows a 1:1 mixture of both cations.

The expected bond-lengths values were calculated by using the tabulated Shannon ionic radii considering $Fe^{3+}/Mn^{4+}/W^{6+}$ in a purely ionic model. The obtained values were $<B\text{-}O>_{4a} = 2.017$ Å and $<B\text{-}O>_{4b} = 1.993$ Å. From the analysis of the refined bond lengths from Table 2, the octahedra seem to be under a strong compressive stress, since they are considerably shorter than the calculated ones. This issue suggests the presence of a strong

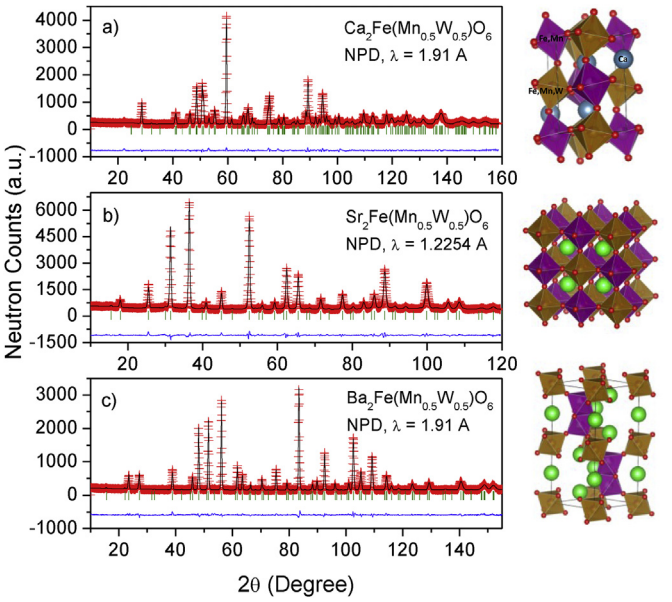

Fig. 2. Observed (circles), calculated (full line) and difference (bottom) profile after a refinement for the three studied samples from high resolution NPD at 295 K data. On the right of the figures the crystal structure representations of each sample are detailed.

covalence at most of the M-O bonds and supports the Mn(IV) oxidation state instead of Mn(II) or Mn(III). The calculated bond distances for these two possible options were markedly higher: For Mn(III): $<B\text{-}O>_{4a} = 2.045$ Å and $<B\text{-}O>_{4b} = 2.0225$ Å and for Mn(II): $<B\text{-}O>_{4a} = 2.0894$ Å and $<B\text{-}O>_{4b} = 2.0706$ Å. Moreover, the absence of oxygen vacancies, microscopically determined from the refinement, supports the presence of Mn(IV) instead of Mn(II) or Mn(III).

3.1.3. *$Ba_2Fe(Mn_{0.5}W_{0.5})O_6$*

The symmetry of the perovskite structure is strongly influenced by the difference in sizes of the cations A and B. In the present case, the A = Ba perovskite presents a tolerance factor of t = 1.05, due to the bulky size of Ba and, therefore, the system tends to evolve to a hexagonal symmetry, in which part of the octahedra happen to share faces instead of vertices. The prototype of the hexagonal distortion in perovskites is found in one of the $BaTiO_3$ polymorphs. It is a laminar structure whose unit cell contains 6 layers of BO_6 octahedra, so they are called 6H-type perovskites. Its structure contains dimeric units of octahedra sharing faces, interspersed between octahedral layers with common vertices to the dimers, and defined in the space group $P6_3/mmc$ (No. 194). In double perovskites, this arrangement contains 2 different cations in the B sublattice, in octahedral positions with a 2: 1 ratio. Therefore, it is ideal for perovskites with formula $A_3B_2B'O_9$, which naturally possess twice as many B cations as B′ cations. However, it can also be adopted by double perovskites with relation B: B′ = 1: 1. In this case there is an intrinsic disorder at least over the nominal position B′, which contain 1/3 of the octahedral atoms.

In the present case of $Ba_2Fe(Mn_{0.5}W_{0.5})O_6$, the structure was refined from NPD data at room temperature in the hexagonal space group $P6_3/mmc$, Z = 3, with a = 5.7408 (1) Å and c = 14.0538 (3) Å. In this space group there are two independent positions for Ba cations; Ba1 located at 2b (0,0,1/4) and Ba2 at 4*f* (1/3, 2/3, z) sites. There are two different crystallographic positions for atoms at B position, with different multiplicity: 2*a* (0,0,0) and 4*f* (1/3, 2/3, z); and there are two types of oxygen atoms in 6 h (x, 2x, 1/4) and 12 k (x, 2x, z) positions.

Fig. 2c shows the Rietveld refinement plot and the right panel displays a view of the hexagonal structure of $Ba_2Fe(Mn_{0.5}W_{0.5})O_6$. It is important to note that $(Fe,Mn)_{4f}O_6$ octahedra (where Fe or Mn are at 4*f* sites) share faces through O1 oxygens; these dimers are connected along the c axis by a single octahedral sheet of $(Mn,Fe,W)_{2a}O_6$ (at 2*a* sites). The degree of disorder between both kind of 2*a* and 4*f* octahedra was refined, assuming that some of the Mn atoms of the 4*f* sites could replace the Fe atoms of 2*a* sites, and vice-versa, constrained to the initial stoichiometry Fe:Mn = 1:0.5. W was always kept at 4*f* sites. The final crystallographic stoichiometry was $Ba_3(Fe_{0.80(1)}Mn_{0.20(1)})_{2a}$ $(Fe_{0.70(1)}Mn_{0.55(1)}W_{0.75})_{4f}O_9$ after refining the structure at room temperature. The bond lengths analysis shows a similar trend as that observed for the Sr sample, were the presence of Mn(IV) instead of the (II) and (III) species is suggested. The dimeric units show an average bond distance of 1.985 Å against 2.014 Å obtained for the vertex-sharing octahedra; the tabulated ionic radii for the cations are $^{VI}Fe^{3+} = 0.645$ Å, $^{VI}Mn^{4+} = 0.53$ Å and $^{VI}W^{6+} = 0.60$ Å. The expected bond distances were $<B\text{-}O>_{2a} = 2.022$ Å and $<B\text{-}O>_{4f} = 1.9965$ Å. From these it seems plausible a higher W and Mn occupancies at the dimeric sites. A strong covalent contribution is suggested for these bonds, manifested by the presence of a compressive stress, as it was observed for the Sr and Ca samples.

In the B_2O_9 dimers, the B ions are displaced from the center of the octahedra along opposite directions, to give B–B distances of 2.847 (6) Å. The similar phenomenon was observed in the ruthenium analogues and in structurally related oxides consisting of M_2O_9 dimers [18–22], which may be caused by the electrostatic repulsion of M ions within the M_2O_9 dimer. The B–O bonds are distorted to accommodate the displacement of B ions: the B–O bond in the face-sharing octahedra are longer than those to the oxygens at the top or bottom of the dimer. Moreover, the shortening of the O2-O2 distances at the common faces of the dimer contributes to the shielding of the B-B electrostatic repulsion. From the analysis of this structure, one question can come to mind: If there are B-B repulsions, why the highly charged W^{6+} atoms occupy these sites, since it seems energetically more favourable for the whole system that the less charged atoms are located at those sites. However, the presence of a d^0 element at the dimers could stabilize the displaced configuration, since i) the occurrence of second-order Jahn Teller distortion and ii) the formation of stronger and weaker B-O bonds could reduce the energy of this repulsive configuration, by removing the degeneracy of the bonds at the B_2O_9 dimer.

3.2. Low temperature evolution: crystal structure and magnetic behavior

Fig. 3 illustrates the χ *vs*. T curves for the $A_2Fe(Mn_{0.5}W_{0.5})O_6$ (A = Ca (a), Sr (b), Ba (c)). The three samples show similar behaviours with small values of susceptibility at low temperature, typically observed in chemically disordered systems. The zero field cooled (ZFC) susceptibility shows a maximum below 50 K, symptomatic of the establishment of long range magnetic ordering, whereas the field cooled (FC) susceptibility reaches a plateau below this temperature. This thermomagnetic irreversibility between ZFC and FC curves, suggests canting of the ordering magnetic moments, or cluster glass-like behavior. This divergence has been previously reported in analogous double perovskites due to the competition of the different magnetic interactions between the different magnetic cations, which hinders the establishment of a long-range ordered magnetic arrangement [23].

Moreover, these phases do not follow a Curie-Weiss law even near room temperature, suggesting the presence of magnetic interactions even at RT. This issue could be associated with the formation of magnetic nanoregions rich in Fe(III) at both octahedral sites, where the magnetic interactions start occurring at markedly higher temperatures, as it happens in $LaFeO_3$ [24]. The difference with that example is that here the extension of these regions probably does not allow a long range magnetic ordering, at least until the establishment of Fe-O-Mn interactions at lower temperatures. The magnetization *vs* magnetic field cycles at 5 K (Fig. 3d) shows a non-negligible hysteresis, which indicates the presence of weak ferromagnetic interactions, perhaps mediated by double exchange between neighboring Fe^{3+} and Mn^{4+} ions.

In order to study the microscopic origin of the magnetic behavior we have collected NPD patterns down to 2 K for the Ca and Sr samples. Both perovskites maintain the same crystal structure in the studied temperature range. Fig. 4 shows the thermal evolution of the neutron diffraction patterns for both oxides. The Ca specimen sample shows a gradual growth of previously existent reflections, below 180 K approximately; while the Sr sample does not show neither additional peaks nor reductions of symmetry in the entire temperature range. However, some interesting peculiarities could be highlighted for both oxides:

3.2.1. CFMW

Upon cooling, two tinny peaks at $2\theta = 33^\circ$ ($d_1 = 4.45$ Å) and $2\theta = 43^\circ$ ($d_2 = 3.44$ Å) grow restrainedly in intensity as temperature decreases; these peaks coincide with some of the crystal structure reflections, as displayed at Figs. 4 and 5. Those peaks suggest the development of a long-range antiferromagnetic ordering. The magnetic structure has been modeled as a G-type antiferromagnetic (AFM) cell, characterized by a propagation vector k = [0 0 0], in which the magnetic moments located on the B sites are oriented almost parallel to the **a**-axis with a small component along the **c** axis, while no component along **b** was observed (See the inset of Figs. 5 and 6). The spins are antiferromagnetically coupled to the six nearest neighbors (disregarding, so far, the presence of randomly distributed non-magnetic W^{6+} ions). The refinements were carried out with some constrains, given the great disorder and the very low intensity of the magnetic reflections. By this way, we have refined the spins in both sites with the same magnitude. As mentioned, there is no evidence of a **b**-component of the spins. Fig. 7 shows the thermal evolution of the unit-cell parameters, volume and magnetic moment components for the sample.

The long range magnetic ordering is observed below 175 K. Fig. 7a shows the second derivative curve of the magnetic susceptibility (in red) together with the unit-cell volume thermal evolution. Two events marked with black vertical lines are observed. The first one is characterized by a slope change of the unit-cell volume evolution at 175 K, coincident with the deviation from zero of the susceptibility derivative curve and the start of the long-range magnetic ordering, as it is remarked at Fig. 5a by the growth of the mentioned reflections. The refined magnetic moments have the main component along the **a** axis while there is no **b**-component. The interaction along **b** is more intense than the other two ones, generating a greater resistance to contraction, actually the **b** parameter remains almost unchanged from 175 to 2.4 K (magnetrostrictive effect). The second event occurs at 50 K. At this point there is a 0.5% drop of the unit-cell volume. This compression mainly occurs along the **c** axis, which in fact is the only parameter suffering a contraction at this temperature. After this axis compression, the **c**-component of the magnetic moment starts disappearing, to give a null **c**-component at 2.4 K. Finally, the most compressible parameter is the **a**-axis, where finally the whole magnitude of the magnetic moment lies. The decreasing rate of the **c**-component is almost the same as the increasing rate of the **a**-component below 50 K, which means that the system is tending to an **a**-axis-collinear arrangement of interacting spins.

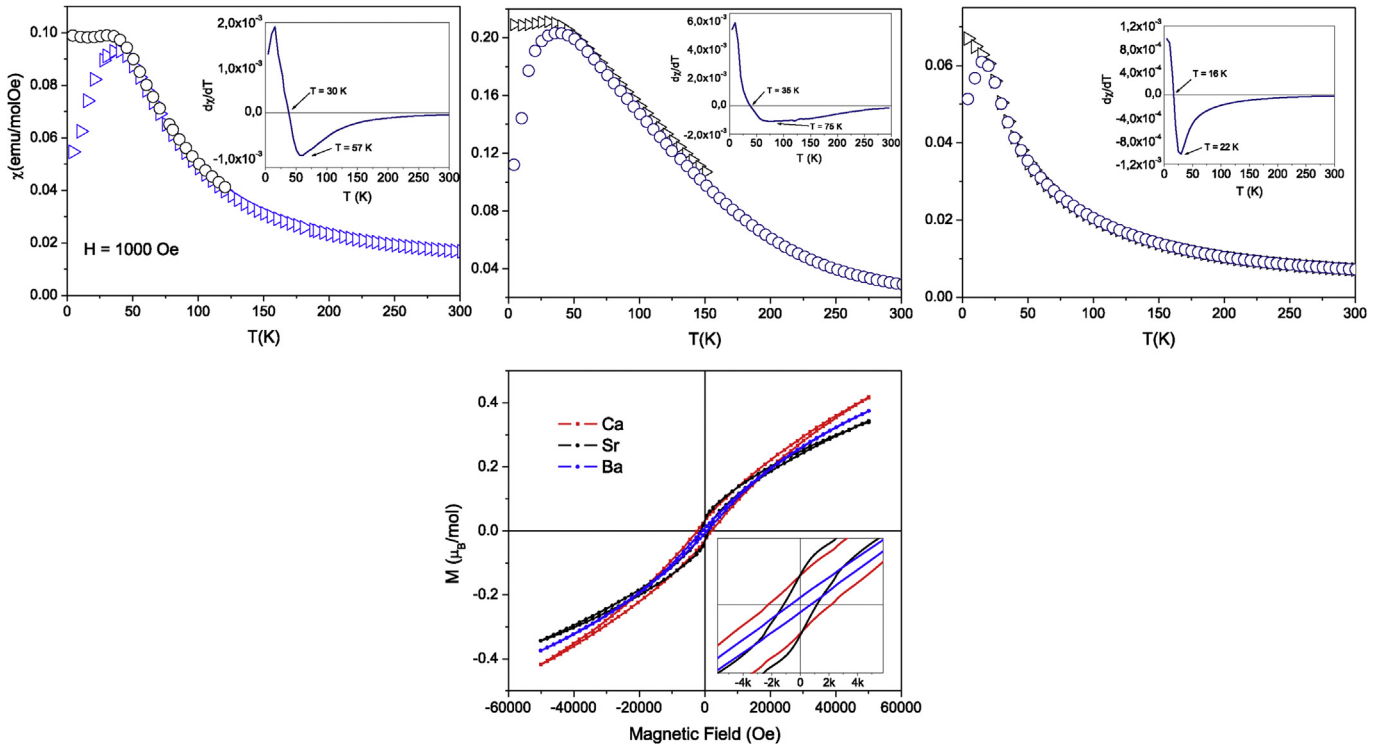

Fig. 3. Thermal evolution of the magnetic susceptibility: field cooling (black markers) and zero field cooling (blue markers). The inset shows the derivative curve of the susceptibility. For A = Ca (a), Sr (b) and Ba (c). d) Magnetization *vs* magnetic field isotherms (T = 5 K) for A = Ca (Red), Sr (Black) and Ba (Blue). (For interpretation of the references to color in this figure legend, the reader is referred to the Web version of this article.)

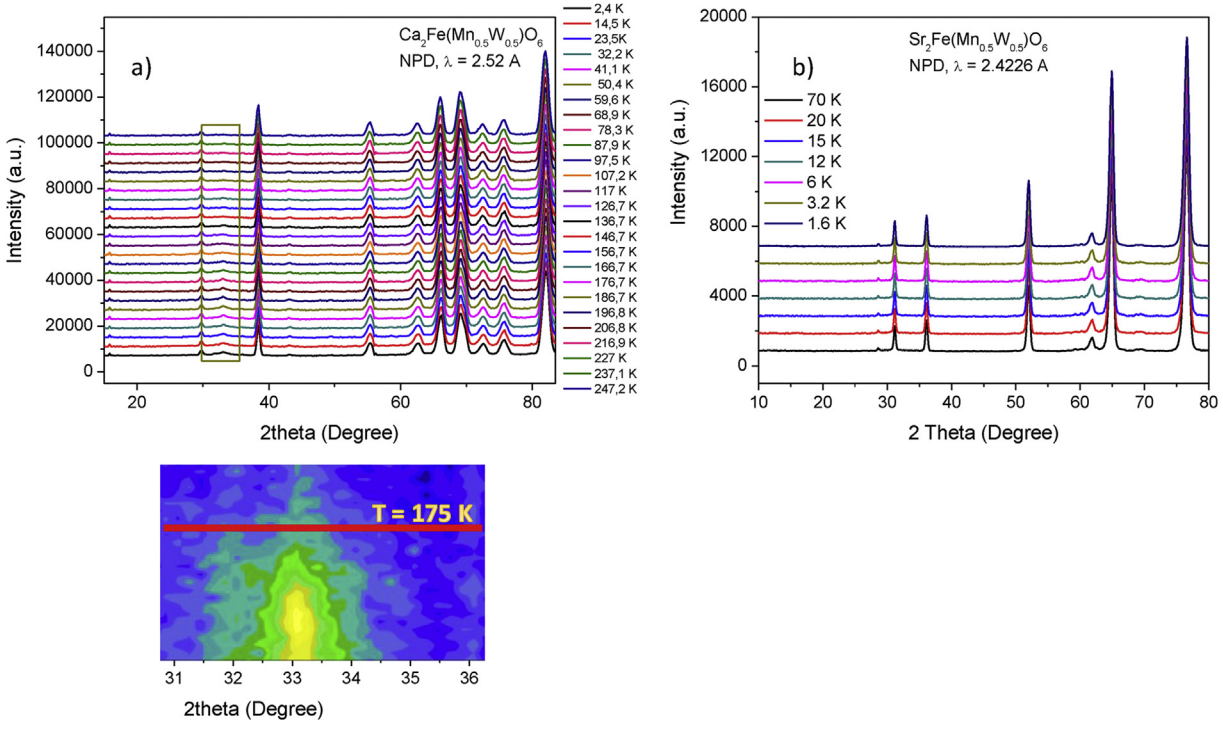

Fig. 4. Low temperature evolution Neutron powder diffraction Patterns collected for the samples with A = Ca (Left) and Sr (Right).

Unfortunately, since our low temperature data are collected with a long wavelength, the refinement of the oxygen positions in the complex monoclinic structure is not possible, so we are not able to obtain accurate information about the bond lengths and angles across these singular events. Synchrotron X-ray diffraction and/or Neutron Powder diffraction with shorter lambda would be very

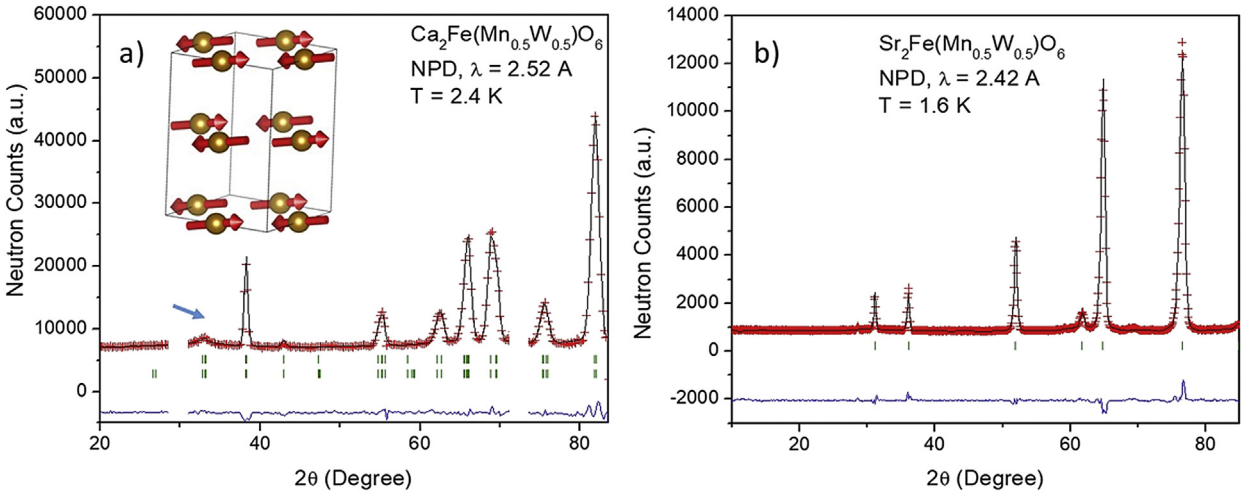

Fig. 5. Observed (circles), calculated (full line) and difference (bottom) profiles after the refinement from D1B NPD data at 2.4 K for the Calcium sample and from G4.1-NPD for the Sr-sample at 1.6 K. Inset: schematic representation of the magnetic structure for $Ca_2Fe(Mn_{0.5}W_{0.5})O_6$.

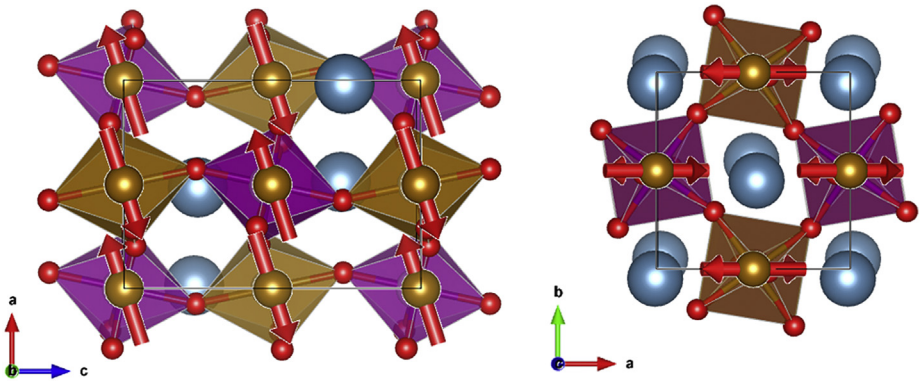

Fig. 6. Schematic representation of the magnetic structure for $Ca_2Fe(Mn_{0.5}W_{0.5})O_6$ a) along the b axis and b) the c axis. The arrows represent the magnetic moments located at the octahedral sites.

helpful to analyze the low-temperature structural behavior of this sample.

3.2.2. SFMW

The low-temperature thermal evolution observed for this sample from NPD shows no evidence of long range magnetic ordering of the spins, even at 1.6 K. However as it was pointed out previously, there is a magnetic event occurring below 50 K at the susceptibility curve. This is characterized by an irreversibility between the FC and ZFC curves, quite possibly mediated by the strong structural chemical disorder between the B-site cations; the separation between the FC and ZFC curves resembles a spin glass or cluster glass behavior. This kind of behavior has been related several times to strongly disordered structures and the presence of very small magnetic domains. Although the magnetic order of the spins occurs only at short range, there is a plausible coupling (as it was observed for the Ca sample) between the magnetic interactions and the crystal structure.

Fig. 5 shows the Rietveld refinement of the lowest temperature pattern, only considering the crystal structure, and Fig. 8 displays the thermal evolution of several parameters of the crystal structure. The unit-cell volume shows a rare behavior below 20 K; in particular the unit-cell volume shows a negative thermal expansion between 10 and 1.6 K. This negative thermal expansion seems to be associated with the octahedral volume of the 4*a* crystallographic site, which is occupied by 70% of Fe and 30% of Mn. The octahedral volume remains almost invariable until 20 K (see Fig. 8); under this temperature down to 10 K there is a marked volume drop, as discussed below. Finally, below 10 K the octahedral volume starts increasing again, suggesting a magnetostrictive effect, where the crystal structure reacts against magnetic frustration by impeding the normal thermal contraction. At the lowest temperature (1.6 K) it reaches almost the initial volume value observed at 70 K. This octahedral volume effect is related to an abrupt oxygen shift along 24e (x, 0,0) positions, and suggests the breathing modes of neighboring octahedra, the 4*a* octahedron contracting and the 4 b octahedron brusquely expanding (Fig. 8). This effect is not well understood so far, although a charge ordering or charge transfer mechanism between neighboring octahedra could be invoked. In any case, this low-temperature sudden contraction-expansion of the octahedral volume had not been previously described in perovskite oxides and certainly deserves more attention utilizing the adequate high-resolution techniques.

4. Conclusions

Three new double perovskites of formula $A_2Fe(Mn_{0.5}W_{0.5})O_6$ (A = Ca, Sr, Ba) have been designed, synthesized and studied. X-ray diffraction (XRD) complemented with Neutron Powder diffraction (NPD) indicate a structural evolution from monoclinic (space group

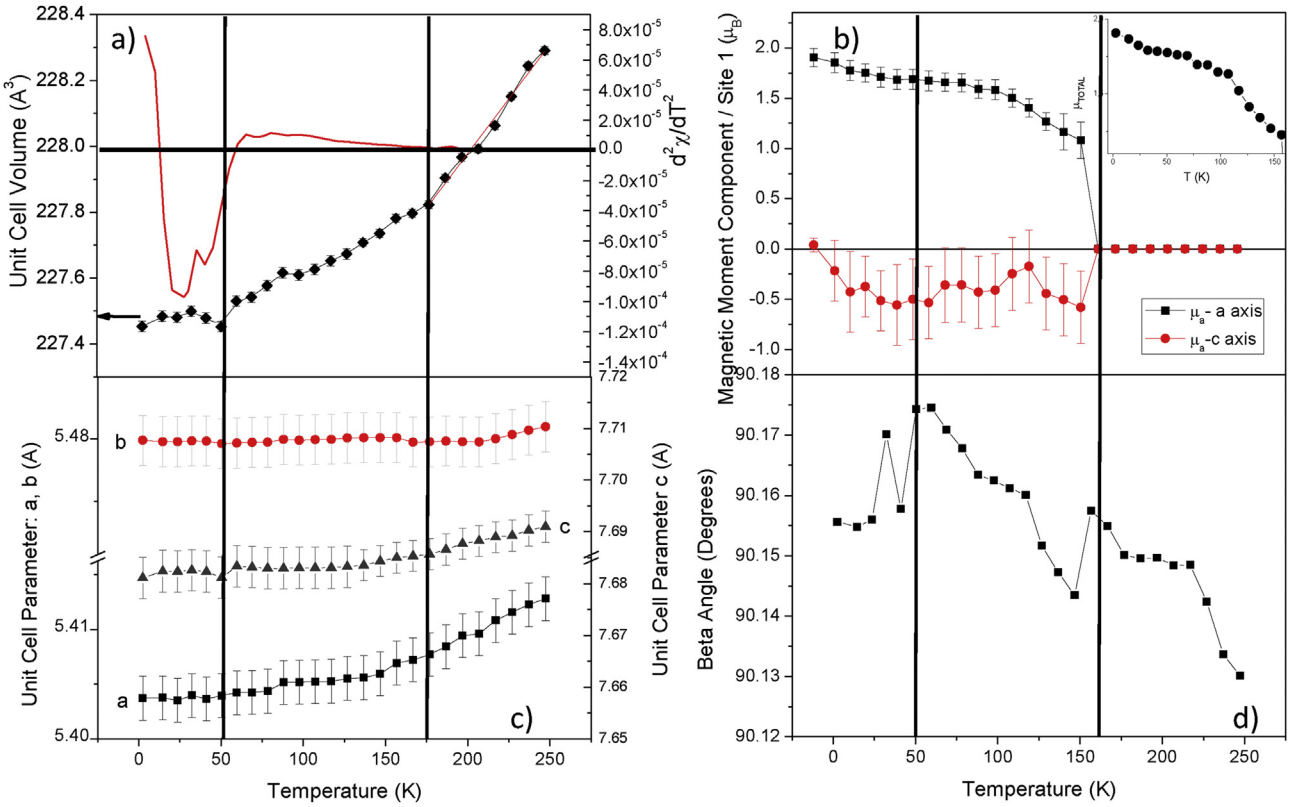

Fig. 7. Thermal evolution of the a) Unit cell Volume (black dots) and $d^2\chi/dT2$ (red line). b) Unit cell parameters: a, b and c. c) The magnetic moment components μ_a (Black markers) and μ_c (Red markers), Inset: Magnitude of the magnetic moment. d) Monoclinic Beta angle. (For interpretation of the references to color in this figure legend, the reader is referred to the Web version of this article.)

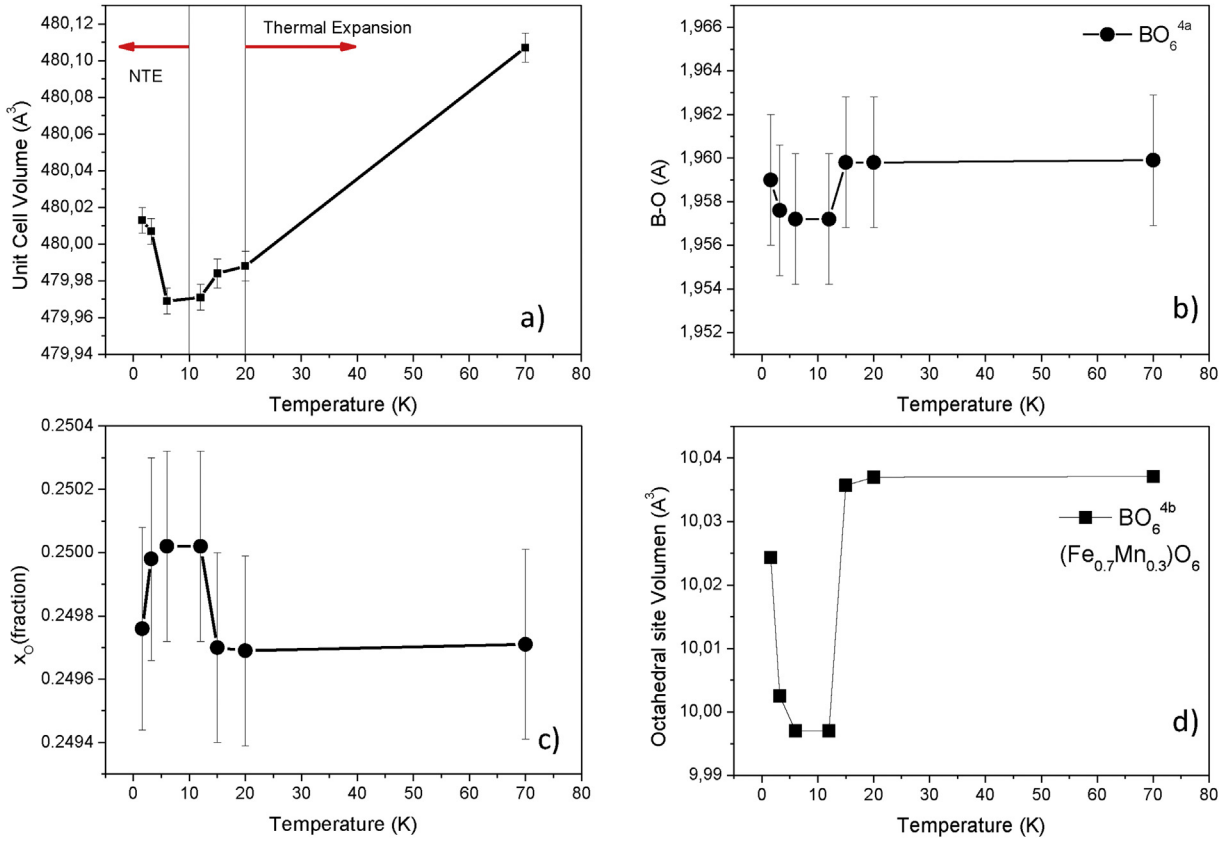

Fig. 8. Thermal evolution of the a) Unit cell Volume (black dots). b) Atomic oxygen refined z coordinate c) B-O distance at the 4*a* crystallographic site. d) Octahedral site Volume.

$P2_1/n$) for A = Ca to cubic ($Fm\text{-}3m$) for A = Sr and finally to hexagonal ($P6_3/mmc$) for A = Ba as the perovskite tolerance factor increases with the A^{2+} ionic size. The three oxides present different tilting schemes of the FeO_6 and $(Mn,W)O_6$ octahedra and all of them show a cationic disorder greater than 70%. This disorder generates very interesting magnetic and structural properties. The three samples show similar behaviors with small values of susceptibility at low temperature, typically observed in chemically disordered systems and a low temperature magnetism ruled by spin or cluster glass states. There is a marked magneto-structural coupling for the Ca sample and an irregular unit-cell volume evolution for the Sr perovskite, finishing with a negative thermal expansion between 10 and 1.6 K suggesting magnetostrictive effects tending to minimize magnetic frustration. It is surprising the great difference observed in the low temperature evolution of the Sr and Ca samples and further experiments will be necessary to map in a very precise way the evolution of the bond lengths and angles across the transitions and to understand the underlying physical mechanism behind these peculiar behaviors.

Acknowledgements

This work was supported by the Spanish Ministry of Economy and Competitivity through grants MAT2017-84496-R. The authors wish to express their gratitude to ILL and LLB for making the facilities available for the neutron diffraction experiments.

References

[1] K.I. Kobayashi, T. Kimura, H. Sawada, K. Terakura, Y. Tokura, Room-temperature magnetoresistance in an oxide material with an ordered double-perovskite structure, Nature 395 (1998) 677.
[2] T.H. Kim, M. Uehara, S.-W. Cheong, S. Lee, Large room-temperature intergrain magnetoresistance in double perovskite $SrFe_{1-x}(Mo \text{ or } Re)_xO_3$, Appl. Phys. Lett. 74 (1999) 1737.
[3] B. García-Landa, C. Ritter, M.R. Ibarra, J. Blasco, P.A. Algarabel, R. Mahendiran, J. García, Magnetic and magnetotransport properties of the ordered perovskite Sr_2FeMoO_6, Solid State Commun. 110 (1999) 435.
[4] A.S. Ogale, S.B. Ogale, R. Armes, T. Venkatesan, Octahedral cation site disorder effects on magnetization in double-perovskite Sr_2FeMoO_6: Monte Carlo simulation study, Appl. Phys. Lett. 75 (1999) 0537.
[5] D. Niebieskikwiat, R.D. Sánchez, A. Caneiro, L. Morales, M. Vásquez-Mansilla, F. Rivadulla, L.E. Hueso, High-temperature properties of the Sr_2FeMoO_6 double perovskite: electrical resistivity, magnetic susceptibility and ESR, Phys. Rev. B 62 (2000) 3340–3345.
[6] O. Chmaissem, R. Kruk, B. Dabrowski, D.E. Brown, X. Xiong, S. Kolesnik, J.D. Jorgensen, C.W. Kimball, Structural phase transition and the electronic and magnetic properties of Sr_2FeMoO_6, Phys. Rev. B 62 (2000) 14197.
[7] B. Martínez, J. Navarro, L. Balcells, J. Fontcuberta, Electronic transfer in Sr_2FeMoO_6 perovskites, J. Phys, Condens. Matter 12 (2000) 10515.
[8] J. Navarro, C. Frontera, L. Balcells, B. Martínez, J. Fontcuberta, Raising the Curie temperature in Sr2FeMoO6 double perovskites by electron doping, Phys. Rev. B 64 (2001), 092411.
[9] M. Retuerto, J.A. Alonso, M.J. Martínez-Lope, J.L. Martínez, M. García-Hernández, Record saturation magnetization, Curie temperature, and magnetoresistancein Sr_2FeMoO_6 double perovskite synthesized by wet-chemistry techniques, Appl. Phys. Lett. 85 (2004) 266–268.
[10] M. Retuerto, M. García-Hernández, M.J. Martínez-Lope, M.T. Fernández-Díaz, J.P. Attfield, J.A. Alonso, Switching from ferro-to antiferromagnetism in A_2CrSbO_6 (A= Ca, Sr) double perovskites: a neutron diffraction study, J. Solid State Chem. 180 (2007) 1582–1589.
[11] R.M. Pinacca, M.C. Viola, J.C. Pedregosa, M.J. Martínez-Lope, R.E. Carbonio, J.A. Alonso, Preparation, Crystal structure and magnetic behaviour of new double perovskites $Sr_2B'UO_6$ with B'= Mn, Fe, Ni, Zn. J. Solid State Chemistry 180 (2007) 1582–1589.
[12] M. Retuerto, J.A. Alonso, M.J. Martínez-Lope, N. Menéndez, J. Tornero, M. García-Hernández, Structural and magnetotransport features in new electron-doped $Sr_{2-x}Ce_xFeMoO_6$ double perovskites, J. Mater. Chem. 16 (2006) 865–873.
[13] H.M. Rietveld, A profile refinement method for nuclear and magnetic structures, J. Appl. Crystallogr. 2 (1969) 65–71.
[14] J. Rodríguez-Carvajal, Recent advances in magnetic structure determination by neutron powder diffraction, Physica B 192 (1993) 55–69.
[15] S.A. Ivanov, S.G. Eriksson, R. Tellgren, H. Rundlof, Structural and magnetic properties of perovskite $Ca_3Fe_2WO_9$, J. Solid State Chem. 178 (2005) 3605–3614.
[16] D. Ballutaud-Harari, P. Poix, J. Solid State Chem. 14 (1975) 354–358.
[17] M. Retuerto, J.A. Alonso, M. Garcıa-Hernandez, M.J. Martınez-Lope, Solid State Commun. 139 (2006) 19–22.
[18] J.T. Rijssenbeek, P. Matl, B. Batlogg, N.P. Ong, R.J. Cava, Electrical and magnetic properties of a series of ternary barium metal ruthenates: Ba3MRu2O9 (M = Fe, Co, Ni, Cu, and In), Phys. Rev. B 58 (1998) 10315–10318.
[19] M.S. Senn, A.M. Arevalo-Lopez, T. Saito, Y. Shimakawa, J.P. Attfield, Nonmagnetic spin-singlet dimer formation and coupling to the lattice in the 6H perovskite Ba3CaRu2O9, J. Phys. Condens. Matter 25 (2013) 496008.
[20] Y. Doi, K. Matsuhira, Y. Hinatsu, Crystal structures and magnetic properties of 6Hperovskites Ba3MRu2O9 (M = Y, In, La, Sm, Eu, and Lu), J. Solid State Chem. 165 (2002) 317–323.
[21] K.E. Stitzer, M.D. Smith, W.R. Gemmill, H.-C. Zur Loye, Novel mixed-valent (V/VI) triple perovskite ruthenates: observation of a complex low-temperature structural and magnetic transition, J. Am. Chem. Soc. 124 (2002) 13877–13885.
[22] C.D. Ling, B.J. Kennedy, Q. Zhou, J.R. Spencer, M. Avdeev, Synthesis, structures, and phase transitions of barium bismuth iridium oxide perovskites Ba2BiIrO6 and Ba3BiIr2O9, J. Solid State Chem. 183 (2010) 727–735.
[23] R. Rodríguez, A. Fernández, A. Isalgue, J. Rodríguez, A. Labrata, J. Tejada, X. Obradors, J. Phys. Chem. 18 (1985) L401.
[24] S.A. Ivanov, S.G. Eriksson, N.W. Thomas, R. Tellgren, H. Rundlof, J. Phys. Condens. Matter 13 (2001) 25.